

The Membrane-Bound Structure and Topology of a Human α -Defensin Indicate a Dimer Pore Mechanism for Membrane Disruption[†]

Yuan Zhang,[‡] Wuyuan Lu,[§] and Mei Hong^{*,‡}

[‡]Department of Chemistry, Iowa State University, Ames, Iowa 50011, United States, and [§]Institute of Human Virology and Department of Biochemistry and Molecular Biology, University of Maryland School of Medicine, Baltimore, Maryland 21201, United States

Received September 16, 2010; Revised Manuscript Received October 20, 2010

ABSTRACT: Defensins are cationic and disulfide-bonded host defense proteins of many animals that target microbial cell membranes. Elucidating the three-dimensional structure, dynamics, and topology of these proteins in phospholipid bilayers is important for understanding their mechanisms of action. Using solid-state nuclear magnetic resonance spectroscopy, we have now determined the conformation, dynamics, oligomeric state, and topology of a human α -defensin, HNP-1, in DMPC/DMPG bilayers. Two-dimensional correlation spectra show that membrane-bound HNP-1 exhibits a conformation similar to that of the water-soluble state, except for the turn connecting strands $\beta 2$ and $\beta 3$, whose side chains exhibit immobilization and conformational perturbation upon membrane binding. At high protein/lipid ratios, rapid ¹H spin diffusion from the lipid chains to the protein was observed, indicating that HNP-1 was well inserted into the hydrocarbon core of the bilayer. Arg C ζ –lipid ³¹P distances indicate that only one of the four Arg residues forms tight hydrogen-bonded guanidinium–phosphate complexes. The protein is predominantly dimerized at high protein/lipid molar ratios, as shown by ¹⁹F spin diffusion experiments. The presence of a small fraction of monomers and the shallower insertion at lower protein concentrations suggest that HNP-1 adopts concentration-dependent oligomerization and membrane-bound structure. These data strongly support a “dimer pore” topology of HNP-1 in which the polar top of the dimer lines an aqueous pore while the hydrophobic bottom faces the lipid chains. In this structure, R25 lies closest to the membrane surface among the four Arg residues. The pore does not have a high degree of lipid disorder, in contrast to the toroidal pores formed by protegrin-1, a two-stranded β -hairpin antimicrobial peptide. These results provide the first glimpse into the membrane-bound structure and mechanism of action of human α -defensins.

Defensins are host-defense antimicrobial proteins present in many animals and plants. These cationic polypeptides contain three intramolecular disulfide bonds, whose linkage patterns distinguish the α -, β -, and θ -defensins (1). Humans have six α -defensins ~30 residues in length (2). Human neutrophil peptides 1–4 (HNP-1–4, respectively) were found in the azurophilic granules of neutrophils (3–5), while HD-5 and HD-6 are present in intestinal epithelial cells (6, 7). Except for HD-6, the human α -defensins show wide-spectrum antimicrobial activities in the microgram per milliliter range (8, 9). Similar to those of many other antimicrobial peptides (AMPs), the general mechanism of antimicrobial action is believed to be permeabilization of the microbial cell membrane (10, 11).

High-resolution crystal structures of all six human α -defensins in the absence of membrane-mimetic solvents have been determined (12, 13). The structures are very similar despite significant sequence differences between HNP-1–3 and the other three defensins. The proteins consist of three antiparallel β -strands ($\beta 1$ – $\beta 3$) connected by turns and a longer loop (Figure 1a). The proteins are dimerized in the crystal through intermolecular H-bonds between the two $\beta 2$ strands, extending the triple-stranded β -sheet to a six-strand β -sheet. The dimer has a basket shape and is amphipathic, with a polar top and an apolar base.

[†]This work was supported by National Institutes of Health Grant GM066976.

*To whom correspondence should be addressed: Department of Chemistry, Iowa State University, Ames, IA 50011. E-mail: mhong@iastate.edu. Telephone: (515) 294-3521. Fax: (515) 294-0105.

On the basis of the crystal structure of HNP-3 (12), several mechanistic models had been proposed to account for the antimicrobial activities of HNPs. The wedge model (12) suggests that the dimer inserts into the bilayer with the hydrophobic bottom contacting the hydrocarbon region of the membrane, thus disrupting lipid packing (Figure 1b,c). The depth of the wedge was unspecified, so the dimer may be partly or completely immersed in the lipid membrane. Alternatively, HNPs might form membrane-spanning pores with the hydrophobic base facing the lipids. In the so-called “dimer pore” model (12) (Figure 1d), the polar tops of two dimers are oriented to favor the transmembrane (TM) orientation of a small solvent channel observed at the dimer interface in the crystal structure (12). In the “general pore” model (12), the dimers are rotated by 90° around the horizontal axis (Figure 1e), so that the side view, parallel to the membrane normal, shows the basket shape of the dimer. A multimeric pore model was also proposed on the basis of vesicle leakage and dextran permeability experiments (14). Here six to eight HNP dimers may form a large pore with an inner diameter of 20–25 Å. The dimers are oriented with the long axis of the basket top at ~45° from the bilayer normal, so that the Arg residues are located in two rings separated by ~16 Å along the bilayer normal, promoting favorable electrostatic interactions with the lipid phosphates (Figure 1f).

Despite many crystal structures of HNPs, no high-resolution structure information for membrane-bound HNPs has been reported. To elucidate the mechanism of action of human

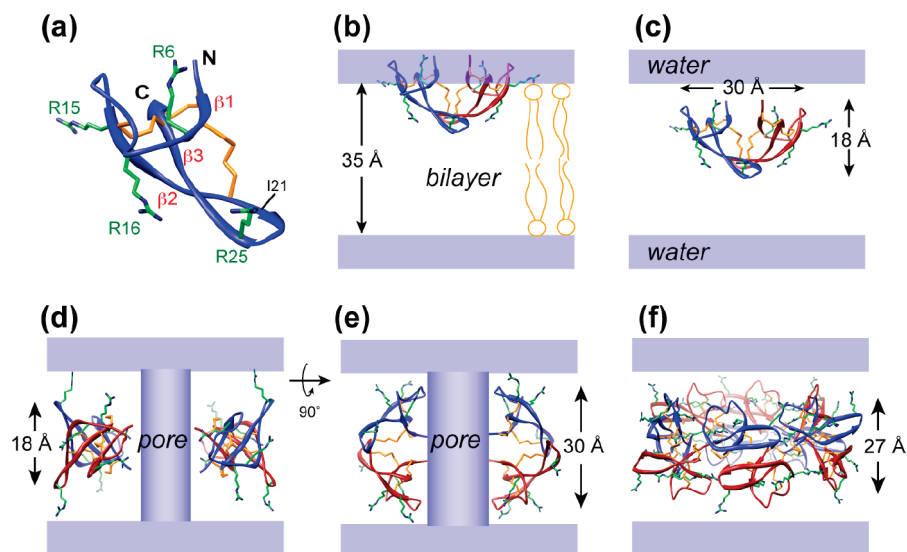


FIGURE 1: Different structural models of HNPs in lipid bilayers. The basic oligomeric state of the protein is a basket-shaped dimer. (a) Structure of the HNP monomer (*I2*) with the four Arg side chains indicated. (b) Surface-bound wedge model with the hydrophobic basket bottom inserted into the bilayer and the polar basket top in contact with water. (c) Membrane-inserted wedge model, in which the hydrophobic basket bottom contacts the lipids while the polar top faces the water pore. (d) Dimer pore model, in which the dimers are rotated by 90° from the dimer pore orientation. (e) General pore model, in which the dimers are rotated by 90° from the dimer pore orientation. (f) Multimeric pore model, in which six dimers form a pore with an ~25 Å inner diameter. The height of the multimer, measured between two Pro8 residues, is 27 Å. The approximate dimensions of the various oligomeric assemblies are given in panels b–f.

defensins, we have initiated a solid-state NMR study of uniformly ^{13}C - and ^{15}N -labeled recombinant HNP-1.¹ Because membrane-bound proteins typically have broader line widths than proteins outside the membrane, due to the conformational disorder of the lipids, we found it necessary to first conduct resonance assignment of the protein in the more ordered water-soluble and lipid-free state. Unlike the bactericidal channel-forming colicins (*I5–I7*), which exhibit abundant membrane-induced dynamics, HNPs cannot undergo large conformational rearrangements because of their multiple disulfide bonds. We thus first determined the NMR structure of lipid-free microcrystalline HNP-1 using two-dimensional (2D) and three-dimensional (3D) magic-angle spinning (MAS) ^{13}C – ^{13}C and ^{13}C – ^{15}N correlation experiments (*I8, I9*). Together with distance constraints, these data led to the first solid-state NMR structure of a human α -defensin, which confirmed the 3D fold seen in the crystal structures (Protein Data Bank entry 2KHT). The NMR structure determination yielded the complete ^{13}C and ^{15}N chemical shifts of the protein (*I9*), with which the membrane-bound HNP-1 chemical shifts can now be compared. In this work, we investigate the conformation and dynamics of HNP-1 in the membrane, its oligomeric state (*20, 2I*), and, most importantly, its interactions with lipids and water. These results yielded the global topology of HNP-1 in the lipid bilayer, allowing us to rule out most structural models and propose the membrane-disruptive mechanism of HNP-1.

MATERIALS AND METHODS

HNP-1 Expression and Synthesis. Recombinant ^{13}C - and ^{15}N -labeled HNP-1 [ACYCRIPACIAGERRYGTCTIYQGRL-WAFCC (Figure 3a)] was obtained as a cleavage product from

its precursor protein, proHNP1. The residues are numbered from A2 to C31 because of sequence alignment with other mammalian defensins, many of which contain an additional N-terminal residue before A2 (*I2*). Using this numbering system also facilitates comparison with HNP-3, which was the first structure determined in the HNP family. Briefly, the expression protocol starts with the expression of proHNP1 as a glutathione *S*-transferase (GST) fusion protein in *Escherichia coli* using ^{13}C - and ^{15}N -labeled Spectra 9 medium (Cambridge Isotope Laboratories) (*I9, 22*). GST-proHNP1 was folded and then cleaved using thrombin, producing proHNP1. ProHNP1 was purified by reversed-phase high-performance liquid chromatography (HPLC) and then cleaved using cyanogen bromide to yield correctly folded HNP-1. Antimicrobial assays confirmed the activity of the protein. For example, 100% killing of *Staphylococcus aureus* is reached at 64 $\mu\text{g}/\text{mL}$ HNP-1 (*I9, 22*). Crude HNP-1 was purified by reversed-phase HPLC. Approximately 1.5 mg of HNP-1 (molecular mass of 3634 Da) was purified from a 1 L culture. ^{19}F -labeled HNP-1 for CODEX experiments was synthesized using *t*-Boc chemistry (*23*), where Tyr4 was replaced with 4- ^{19}F Phg. The use of phenylglycine removes the possibility of side chain χ_1 motion that could complicate the interpretation of the CODEX data (*24, 25*). The choice of Tyr4 as the ^{19}F -labeled site was based on crystal structures of various HNPs, all showing close intersubunit contact of this residue (*I2, I3, 26*). Previous studies of 4- ^{19}F Phg mutants of the related β -hairpin antimicrobial peptide, PG-1 (*24*), suggest that the mutation generally does not perturb the antimicrobial activities of the peptides.

Membrane Sample Preparation. DMPC and DMPG lipids (Avanti Polar Lipids, Alabaster, AL) were codissolved in chloroform at a molar ratio of 3:1, dried under a stream of nitrogen gas, redissolved in cyclohexane, and lyophilized overnight. The dry and homogeneous lipid powder was suspended in a pH 7 phosphate buffer, vortexed, and then subjected to five freeze–thaw cycles. The vesicle solution was then extruded through polycarbonate filters with pore sizes of 400 and 100 nm to obtain large

¹Abbreviations: HNP-1, human neutrophil peptide 1; DMPC, 1,2-dimyristoyl-*sn*-glycero-3-phosphatidylcholine; DMPG, 1,2-dimyristoyl-*sn*-glycero-3-phosphatidylglycerol; MAS, magic-angle spinning; CP, cross-polarization; DARR, dipolar-assisted rotational resonance; DIPSHIFT, dipolar-chemical-shift; REDOR, rotational-echo double resonance.

unilamellar vesicles. HNP-1 was dissolved in 1 mL of phosphate buffer, added to the lipid vesicle solution, and dialyzed overnight. The mixture was centrifuged at 200000g for 3 h at 4 °C to obtain a membrane pellet. The pellet was pipet-transferred into 4 mm MAS rotors for NMR experiments.

Three samples were prepared: two [U-¹³C, ¹⁵N]HNP-1 samples at protein:lipid (P:L) molar ratios of 1:18 and 1:40 and one ¹⁹F-labeled HNP-1 sample at a P:L ratio of 1:18. The 1:18 molar ratio corresponds to a mass ratio of 1:3.3; thus, there was sufficient lipid to ensure appropriate protein–lipid interactions.

Solid-State NMR Spectroscopy. Most 2D resonance assignment experiments were conducted on a Bruker (Karlsruhe, Germany) AVANCE-600 (14.1 T) spectrometer operating at a ¹³C Larmor frequency of 150.92 MHz. A Bruker DSX-400 (9.4 T) spectrometer was used for ¹³C–³¹P REDOR experiments, ¹H spin diffusion, and ¹³C–¹H dipolar coupling measurements. Triple-resonance MAS probes with 4 mm rotors were used for all experiments. ¹³C and ³¹P chemical shifts were referenced externally to the α-glycine ¹³CO signal at 176.49 ppm on the TMS scale and the hydroxyapatite ³¹P signal at 2.73 ppm on the phosphoric acid scale, respectively. ¹⁵N chemical shifts were referenced to the ¹⁵N signal of *N*-acetylvaline at 122.0 ppm on the liquid ammonia scale.

2D ¹³C–¹³C DARR correlation spectra (27) were recorded at 273 K under 5 kHz MAS with a ¹³C spin diffusion time of 40 ms. 2D N(CO)CX and N(CA)CX correlation spectra (28, 29) were recorded at 273 K under 7.5 kHz MAS with a ¹³C mixing time of 40 ms for NCACX and 60 ms for NCOCX. The ¹⁵N–¹³C SPECIFIC (30) cross-polarization (CP) contact times were 3 ms. In the intraresidue NCACX experiment, ¹⁵N–¹³Cα magnetization transfer was achieved using a ¹⁵N spin-lock field of 17 kHz and an on-resonance ¹³Cα spin-lock field of 25 kHz. In the inter-residue NCOCX experiment, ¹⁵N–¹³CO magnetization transfer was accomplished with a ¹⁵N on-resonance spin-lock field of 27 kHz and a tilted ¹³CO spin-lock field strength of 35 kHz, which was the result of a 30 kHz applied field on resonance with Cα and an 18 kHz offset for CO.

¹³C–¹H dipolar couplings were measured at 303 K using the 2D dipolar-chemical-shift (DIPSHIFT) correlation experiment (31). The sample was spun at 4.5 kHz, and the MREV-8 sequence (32) was used for ¹H homonuclear decoupling. The *t*₁ curves were fit using a Fortran program, and the fit values were divided by the MREV-8 scaling factor to yield the true couplings. To account for uncertainties in the MREV-8 scaling factor, we measured the rigid-limit C–H dipolar couplings using the crystalline model peptide formyl-Met-Leu-Phe (f-MLF) (33, 34), where Leu Cα, Met Cβ, and Leu Cδ signals represented CH, CH₂, and CH₃ groups, respectively. The CH and CH₂ peaks gave C–H rigid-limit dipolar couplings of 11.2 kHz (fit values), which corresponded to true couplings of 23.8 kHz when the theoretical scaling factor of 0.47 for MREV-8 was used (35). For the Leu CH₃ signal, the fit value was 3.5 kHz. The ratio of the measured HNP-1 couplings with the rigid-limit f-MLF couplings yielded order parameter *S*_{CH}.

To determine the depth of insertion of HNP-1, we conducted 2D ¹³C-detected ¹H spin diffusion experiments (36, 37) at 303 or 308 K under 5 kHz MAS. For the 1:18 P:L ratio sample, ¹H spin diffusion mixing times (*t*_m) of 2.25–225 ms were applied to transfer the ¹H magnetization of mobile lipids and water to HNP-1. For the 1:40 P:L ratio sample, two mixing times of 100 and 225 ms were measured because the sensitivity was too low to measure a complete buildup curve. The ¹H magnetization transfer was

detected through the protein ¹³C signals. To ensure that only the mobile lipid and water polarization served as the ¹H magnetization source, we suppressed the ¹H magnetization of the rigid protein with a ¹H *T*₂ filter of 0.4 × 2 ms before the *t*₁ evolution period. For the 2.25 ms spectrum of the 1:18 sample, the water ¹H cross section was extracted to analyze the water-proximal residues in the protein.

A frequency-selective rotational-echo double-resonance (REDOR) experiment (38) was used to measure distances from protein ¹³C atoms to lipid ³¹P atoms. The experiments were performed at 233 K under 4.5 kHz MAS to suppress lipid motions as well as protein side chain motions. A rotor-synchronized ¹³C Gaussian 180° pulse of 444 μs was applied in the middle of the REDOR period to suppress ¹³C–¹³C *J* couplings between the on-resonance ¹³C and its directly bonded spins. ³¹P 180° pulses of 9 μs were applied every half-rotor period to recouple the ¹³C–³¹P dipolar coupling. The time-dependent REDOR intensities were fit using two-spin simulations, which had been shown (39) to correspond to the vertical distance between the ¹³C spin and the ³¹P plane for long distances of more than ~6 Å.

¹⁹F CODEX experiments (20, 40, 41) for determining the oligomeric state of HNP-1 were conducted at 233 K under 7 kHz MAS. The ¹⁹F chemical shift anisotropy (CSA) was recoupled by two rotor periods of 180° pulses. During the mixing time, ¹⁹F spin diffusion changes the ¹⁹F CSA and prevents complete refocusing of a stimulated echo. A z-filter after the second 180°-pulse train allows the correction of ¹⁹F *T*₁ relaxation effects by conducting two experiments for each *t*_m, a control experiment (*S*₀) in which the short z-filter period (10 μs) was applied between the two 180°-pulse trains while the long *t*_m occurred afterward and a dephasing experiment (*S*) in which the long *t*_m occurs between the two 180°-pulse trains. The intensity ratio, *S*/*S*₀, at equilibrium yields the number of ¹⁹F spins in the proximity. Two mixing times, 500 ms and 1 s, were measured.

RESULTS

Conformation and Dynamics of HNP-1 in the Lipid Membrane. Panels a and b of Figure 2 show the ³¹P spectrum of the DMPC/DMPG (3:1) membrane with bound HNP-1 above (303 K) and below (253 K) the membrane phase transition temperature. At 303 K, the ³¹P spectrum has the classical uniaxial line shape indicative of lamellar bilayers and is identical to the protein-free lipid spectrum, indicating that HNP-1 does not cause observable orientation disorder to the lipid bilayer. Below the phase transition temperature (23 °C), the ³¹P spectrum exhibited the expected broadening, with a rigid-limit span of 210 ppm at 253 K.

We examined the membrane-bound conformation of HNP-1 by first comparing the one-dimensional (1D) ¹³C spectra of the membrane-bound and microcrystalline states. Panels c and d of Figure 2 show the ¹³C spectra of DMPC/DMPG membrane-bound HNP-1 at 298 and 273 K. The intensity and line widths were largely unaffected by temperature, suggesting that HNP-1 was immobilized at ambient temperature. Compared to the microcrystalline protein spectrum (Figure 2e), that of the membrane-bound sample exhibited similar intensity distributions except for the additional lipid peaks. Thus, HNP-1 adopts a similar overall conformation in the membrane as in the microcrystalline state, as expected for this disulfide-bonded protein.

To better resolve the resonances, we measured 2D ¹³C–¹³C and ¹⁵N–¹³C correlation spectra. The 2D ¹³C–¹³C DARR spectrum at 40 ms mixing (Figure 3b) showed mostly intraresidue

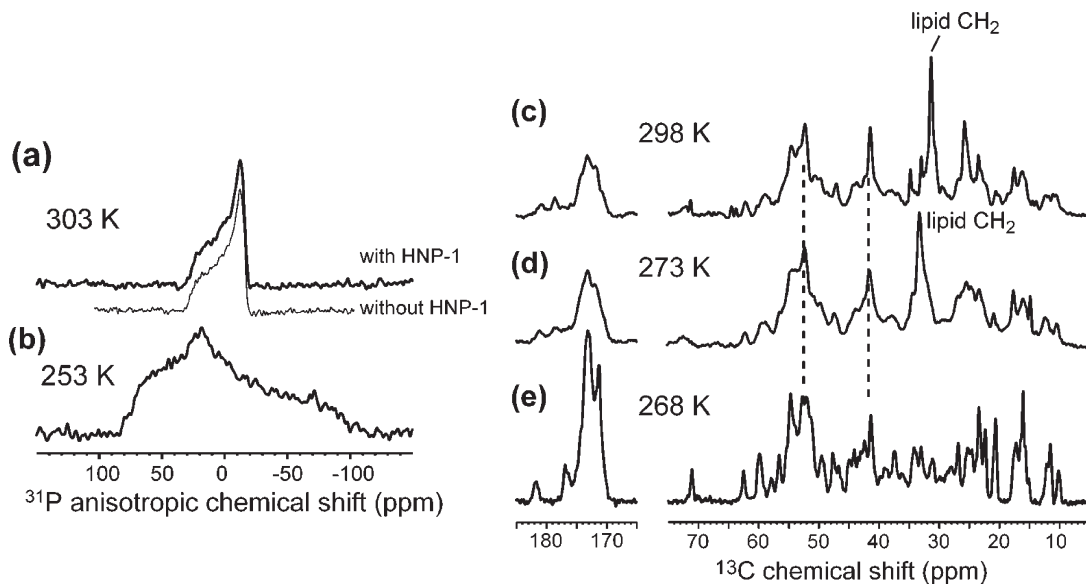


FIGURE 2: One-dimensional ^{31}P and ^{13}C spectra of membrane-bound HNP-1. (a) ^{31}P static spectra of DMPC/DMPG membranes with HNP-1 (1:18 P:L ratio) (thick line) and without HNP-1 (thin line), measured at 303 K. The protein-bound spectrum exhibits no isotropic peak and is identical to the non-protein-containing spectrum. (b) ^{31}P spectrum of the HNP-1-bound DMPC/DMPG membrane at 253 K. (c and d) ^{13}C MAS spectrum of membrane-bound HNP-1 at 298 K (c) and 273 K (d). The intensities and line widths are little affected by temperature, indicating that HNP-1 is immobilized in the liquid-crystalline membrane. (e) ^{13}C spectrum of microcrystalline HNP-1 without the lipids at 268 K. The intensity distribution of the membrane-bound HNP-1 is similar to that of the microcrystalline protein, indicating similar conformations.

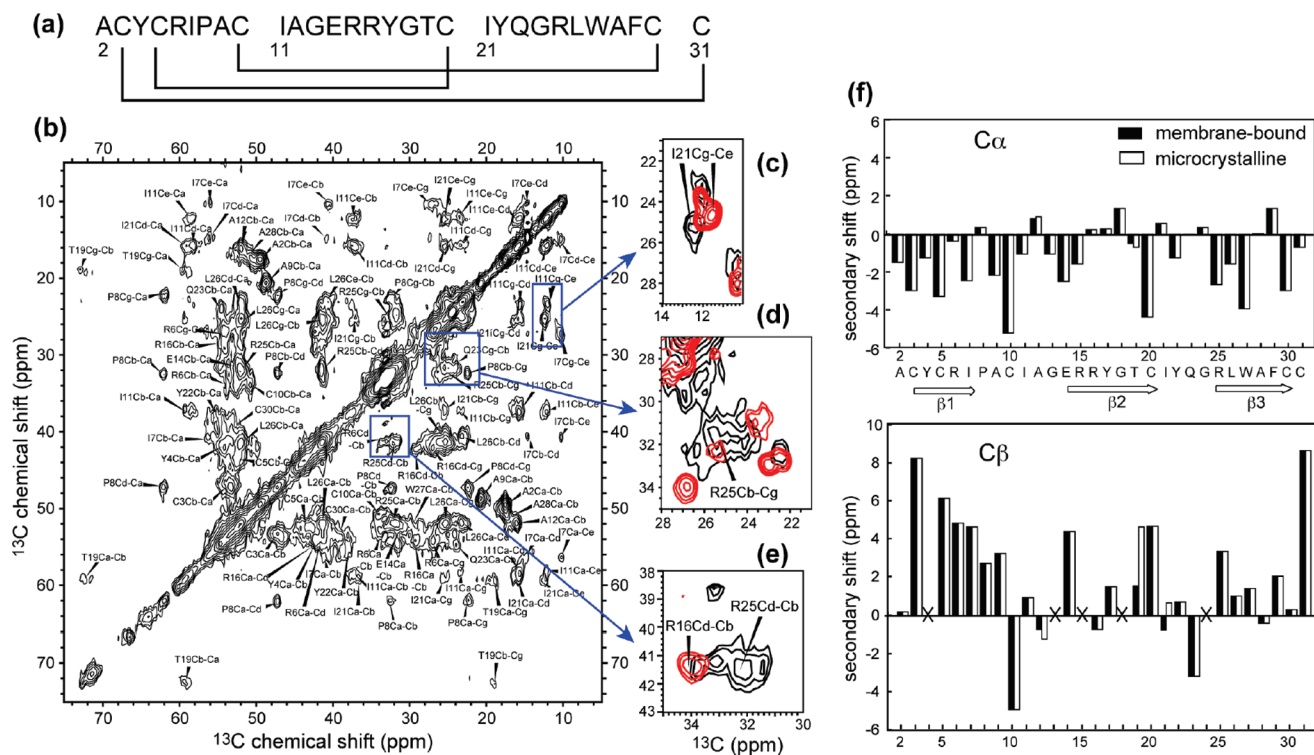


FIGURE 3: Resonance assignment of membrane-bound HNP-1 and comparison with the microcrystalline protein. (a) Amino acid sequence of HNP-1. (b) 2D ^{13}C - ^{13}C DARR spectrum of membrane-bound HNP-1 at 273 K with a mixing time of 40 ms. (c–e) Regions that show chemical shift changes between the membrane-bound (black) and microcrystalline (red) states: (c) I21 side chain, (d) R25 side chain, and (e) R25 and R16 side chains. Note the significant increase in the R25 side chain intensities in the membrane-bound state in panels d and e. (f) $\text{C}\alpha$ and $\text{C}\beta$ secondary chemical shifts of HNP-1 in the membrane-bound and microcrystalline states, confirming the β -strand-rich nature of the protein and the overall similarity of the protein structure in the two states.

cross-peaks, which were readily assigned by comparison with the microcrystalline spectra (19). 2D N(CO)CX and N(CA)CX spectra (Figure S1 of the Supporting Information) further corroborated the assignments. Most residues exhibited similar chemical shifts in the membrane and in the microcrystalline state,

except for the side chains of I21 and R25. The I21 $\text{C}\gamma$ and $\text{C}\epsilon$ peaks moved downfield from the microcrystalline state: the $\text{C}\gamma$ chemical shift increased from 24.6 to 25.5 ppm, while the $\text{C}\epsilon$ peak moved from 11.5 to 12.4 ppm (Figure 3c). In the microcrystalline state, the R25 side chain resonances were not visible in the 2D

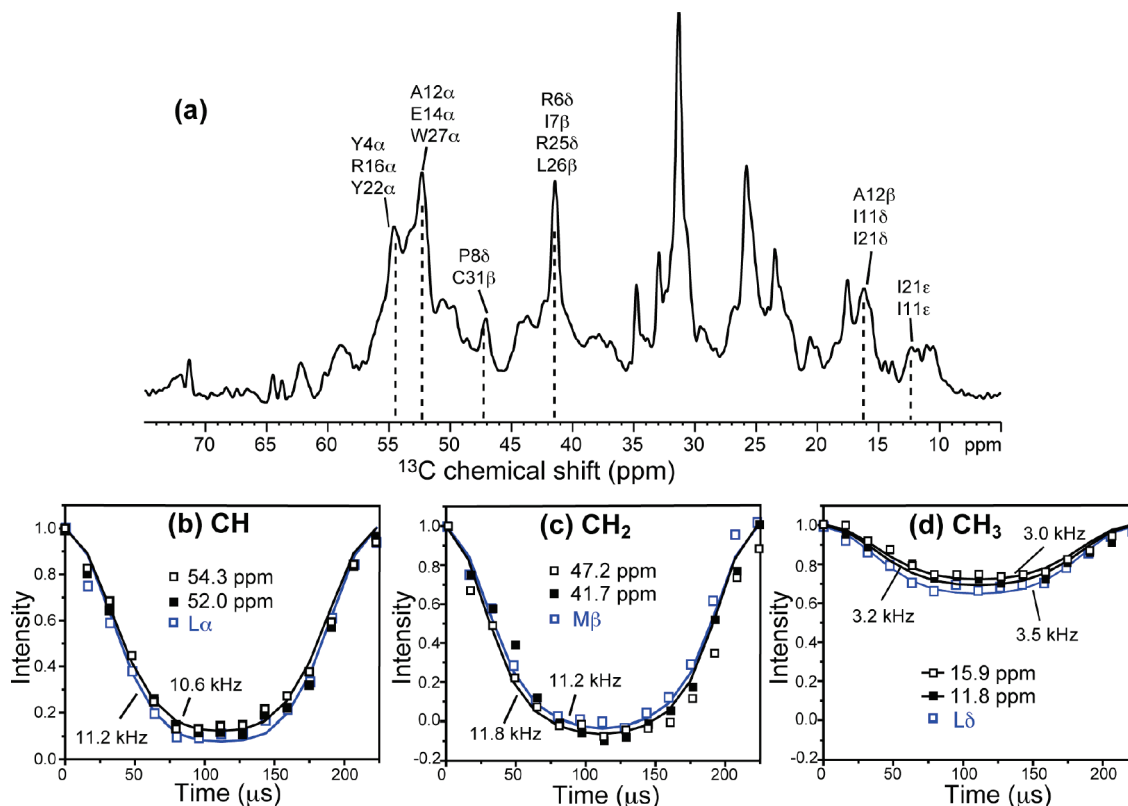


FIGURE 4: ^{13}C – ^1H dipolar couplings of DMPC/DMPG membrane-bound HNP-1 at 303 K under 4.5 kHz MAS. (a) ^{13}C chemical shift dimension of the 2D spectrum. (b) C–H dipolar coupling curves of two $\text{C}\alpha$ cross sections and their best fit, compared with the Leu $\text{C}\alpha$ data of f-MLF. (c) C–H dipolar coupling curves of two CH_2 peaks and their best fit, compared with the Met $\text{C}\beta$ data of f-MLF. (d) C–H dipolar coupling curves of two CH_3 cross sections and their best-fit simulations at 3.0 and 3.2 kHz, compared to the Leu $\text{C}\delta$ signal of f-MLF. All couplings here are fit values and convert to true couplings after being divided by the homonuclear decoupling scaling factor.

^{13}C – ^{13}C spectrum and much weaker than the R6 and R16 signals in the 3D NCC spectra (19). In comparison, in the membrane-bound state, the R25 side chain resonances became much stronger, with clear $\text{C}\beta$ – $\text{C}\gamma$ and $\text{C}\delta$ – $\text{C}\beta$ cross-peaks (Figure 3d,e). I21 and R25 are both located near the $\beta 2$ – $\beta 3$ turn at the hydrophobic base of the dimer (Figure 1a). This turn was seen in the HNP-3 crystal structure to deviate significantly from crystallographic symmetry and was thought to exhibit flexing motions (12). Thus, the membrane-induced conformational and dynamical changes of I21 and R25 side chains are likely significant and may reflect site-specific interactions of this $\beta 2$ – $\beta 3$ turn with lipids (see below). Figure 3f shows the $\text{C}\alpha$ and $\text{C}\beta$ secondary chemical shifts (42) of HNP-1 for both the membrane-bound and microcrystalline states, confirming the triple-stranded motif of the protein and the similarity of the protein conformation without and with the lipids. The secondary shifts suggest that the Y17–G18 junction in the middle of the $\beta 2$ strand deviates from the ideal β -sheet structure, as noted previously (19), which may reflect the role of G18 as a hinge for the $\beta 2$ – $\beta 3$ hairpin (13).

To evaluate the mobility of membrane-bound HNP-1 quantitatively, we measured the ^{13}C – ^1H dipolar couplings using the 2D DIPSHIFT experiment. Figure 4 shows the ^{13}C chemical shift dimension of the 2D spectrum, with partial resolution of the sites. Several dipolar cross sections representing the backbone $\text{C}\alpha$ – $\text{H}\alpha$ and side chain CH_2 and CH_3 groups are shown. We obtained rigid-limit S_{CH} values of 0.95–1.05 for $\text{C}\alpha$ and methylene groups, while the methyl groups of Ile and Ala exhibited S_{CH} values of 0.26–0.28. Because methyl three-site jumps alone give an order parameter of 0.33, the small degree of additional scaling, by a factor of 0.78–0.85, indicates that other torsional degrees of

freedom in the aliphatic side chains of these residues are insignificant. Thus, the DIPSHIFT data are consistent with the temperature insensitivity of the ^{13}C spectra and indicate that the HNP-1 backbone is immobilized in the liquid-crystalline phase of the bilayer, and only the side chains exhibit moderate motion. This finding not only is consistent with the conformational rigidity of this disulfide-bonded protein but also more importantly indicates that HNP-1 is not monomeric in the membrane. If the protein were monomeric, the low molecular mass would cause fast whole-body uniaxial diffusion of the protein in the membrane, as observed in many small- and medium-sized membrane proteins with molecular masses of up to several tens of kilodaltons (43–47). Because all HNPs form dimers in the crystal (12, 13, 48), the immobilization suggests that when bound to the membrane, HNP-1 is at least dimeric and may form higher-order oligomers.

Depth of Insertion of HNP-1 from Lipid–Protein ^1H Spin Diffusion. To determine the immersion depth of HNP-1, we conducted a 2D ^{13}C -detected ^1H spin diffusion experiment (36). The experiment measures interproton distances from the mobile water and lipid acyl chains to the rigid protein through distance-dependent ^1H magnetization transfer. TM proteins in contact with both the membrane surface and the hydrocarbon core exhibit fast ^1H spin diffusion from both lipid acyl chains and water (37), while surface-bound proteins have much slower ^1H spin diffusion from the lipid chains.

Figure 5 shows the ^1H spin diffusion data of membrane-bound HNP-1 (1:18 P:L ratio) at 303 K. A representative 2D spectrum (mixing time of 100 ms) shows the characteristic cross-peaks between the protein ^{13}C signals (37–63 ppm) and the lipid CH_2

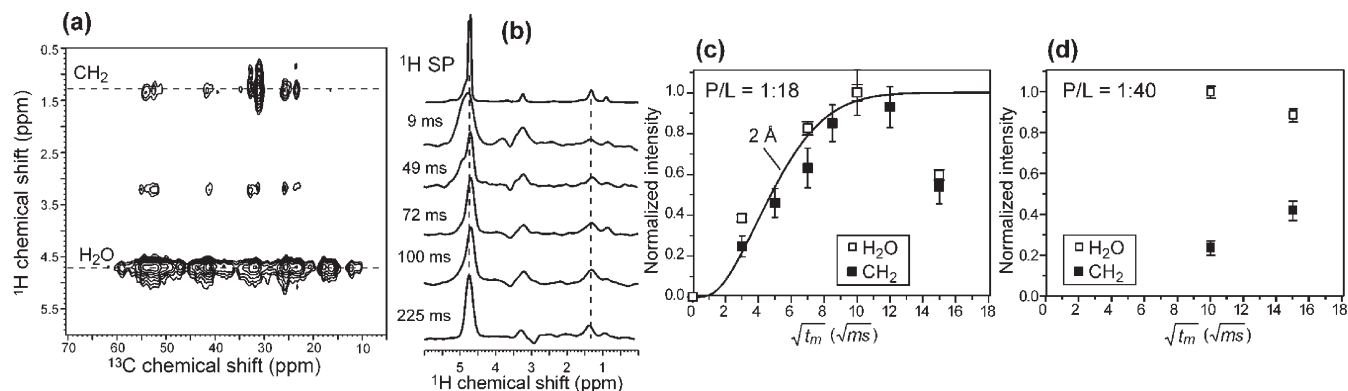


FIGURE 5: ^1H spin diffusion from lipid chains and water to HNP-1 in DMPC/DMPG bilayers. (a) Representative 2D spectrum for a 1:18 P:L ratio at 303 K, with a ^1H mixing time of 100 ms. (b) Integrated ^1H cross sections from ^{13}C chemical shifts of 37–63 ppm as a function of ^1H mixing time, compared with the 1D ^1H spectrum at the top. (c) ^1H spin diffusion buildup curves for lipid CH_2 and water at a 1:18 P:L ratio. (d) ^1H spin diffusion intensities for lipid CH_2 and water at a 1:40 P:L ratio. The CH_2 buildup is much slower at the lower protein concentration.

protons at 1.3 ppm, indicating that HNP-1 is within spin diffusion reach of the acyl chains. Strong water–protein cross-peaks were also observed. To quantify the distances, we measured the 2D spectra as a function of mixing time. Figure 5b shows the integrated ^1H cross sections for ^{13}C chemical shifts of 37–63 ppm for mixing times of 9–225 ms. After correcting for ^1H T_1 relaxation of the water and CH_2 protons, we plotted the cross-peak intensities as a function of the square root of the mixing time. Figure 5c shows that both the water and lipid cross-peaks reached a plateau by 100 ms, qualitatively indicating that HNP-1 is in close contact with both the hydrophobic core of the membrane and water. The equilibration allows both the water and lipid cross-peaks to be normalized with respect to their own maximal intensities at 100 ms.

We simulated the CH_2 buildup curve using a 1D lattice model to obtain the minimum lipid–protein separation. In this model, ^1H magnetization (M_i) transfer was modeled as a discrete process along the bilayer normal (49). The transfer rate ($\Omega = D/a^2$) depends on lattice spacing a , fixed at 2 Å, and the diffusion coefficients of the various membrane components. On the basis of previous calibrations, we used diffusion coefficients of 0.012 nm^2/ms for lipids (D_L), 0.03 nm^2/ms for water (D_W), and 0.3 nm^2/ms for the protein (D_P) (24, 36, 50). For the interfacial D_{LP} between the lipid and the protein, we used a value of 0.0025 nm^2/ms , which was within the range reported previously (24, 36, 50). The simulation yields the minimal lipid–protein or water–protein distances because once ^1H magnetization crosses the interface from the soft lipid matrix (or water) to the nearest protein residues, it is rapidly equilibrated within the immobilized protein. The lack of site specificity allowed us to use the integrated intensities for the protein ^{13}C signals to obtain global information about the depth of insertion of HNP-1. Figure 5c shows that the CH_2 buildup curve for the 1:18 P:L ratio sample was best fit to a distance of 2 Å, indicating that HNP-1 was well inserted into the hydrophobic region of the DMPC/DMPG bilayer, in immediate contact with the acyl chains. This proximity rules out the surface-bound wedge model (Figure 1b): if the basket-shaped dimer is exposed to the aqueous phase to any significant extent, for example one-third of its 18 Å height, then the membrane-immersed part of the protein would be ~ 12 Å, which would make the protein mostly outside the hydrophobic region of the bilayer.

Some antimicrobial peptides have been found to exhibit concentration-dependent interactions with the lipid bilayer: they

bind to the surface of the lipid bilayer at low concentrations but insert into the membrane at high concentrations (51, 52). To determine whether the depth of insertion of HNP-1 changes with concentration, we measured the ^1H spin diffusion spectra at a 1:40 P:L ratio. We measured two mixing times, 100 and 225 ms, which were sufficiently long to give equilibrium intensities for the 1:18 sample. The lipid–protein cross-peaks at 225 ms were clearly higher than at 100 ms after correction for ^1H T_1 relaxation, indicating that the CH_2 cross-peaks had not equilibrated by 225 ms. To obtain the correct normalization, we scaled the CH_2 cross-peak intensities with the water cross-peak intensities in the 100 ms spectrum, because the water intensities were already equilibrated at 100 ms (Figure 5d), consistent with all membrane proteins studied so far (53–55). This ratio was further scaled by the equilibrium intensity ratio (0.61) between the CH_2 peak and the water peak in the 1D ^1H spectrum:

$$I_{\text{CH}_2}^{\text{norm}}(t_m) = \frac{I_{\text{CH}_2}^{\text{obs}}(t_m)e^{t_m/T_{1,\text{CH}_2}}}{(I_{\text{H}_2\text{O}}^{\text{obs},100\text{ms}}e^{t_m/T_{1,\text{H}_2\text{O}}})(I_{\text{CH}_2}^{\text{eq}}/I_{\text{H}_2\text{O}}^{\text{eq}})} \quad (1)$$

The normalized CH_2 intensities at a 1:40 P:L ratio are significantly lower than those of the 1:18 sample, indicating that HNP-1 inserts more shallowly at lower protein concentrations. Thus, HNP-1 has concentration-dependent insertion, similar to that of several other antimicrobial peptides (51, 52).

Membrane Topology of HNP-1 from ^{13}C – ^{31}P Distances. To further define the membrane topology of HNP-1, we measured ^{13}C – ^{31}P distances between the Arg residues and the lipid headgroups. The well-resolved Arg $\text{C}\zeta$ signal at 157 ppm provides a site-specific probe of the interaction of the four Arg residues with the lipid phosphates. Figure 6a shows the normalized $\text{C}\zeta$ intensities (S/S_0) as a function of REDOR mixing time. The intensities decayed quickly to 0.67 in the first 10 ms and then more slowly to ~ 0.5 by 18 ms. The bimodal decay cannot be fit to a single distance but to a short distance of 4 Å for the initial fast regime and three longer distances of ~ 7 Å for the long-time regime. The weighting factor of 1:3 reflects the intensity plateau at 0.67 between 8 and 14 ms. Thus, the data suggest that one of four guanidinium ions forms tight H-bonded complexes with the lipid phosphates, while the other three Arg residues are more distant.

We now consider the compatibility of the various membrane topological models of HNP-1 with the Arg $\text{C}\zeta$ –P distances. In the fully immersed wedge model (Figure 6b), R6 and R15 are

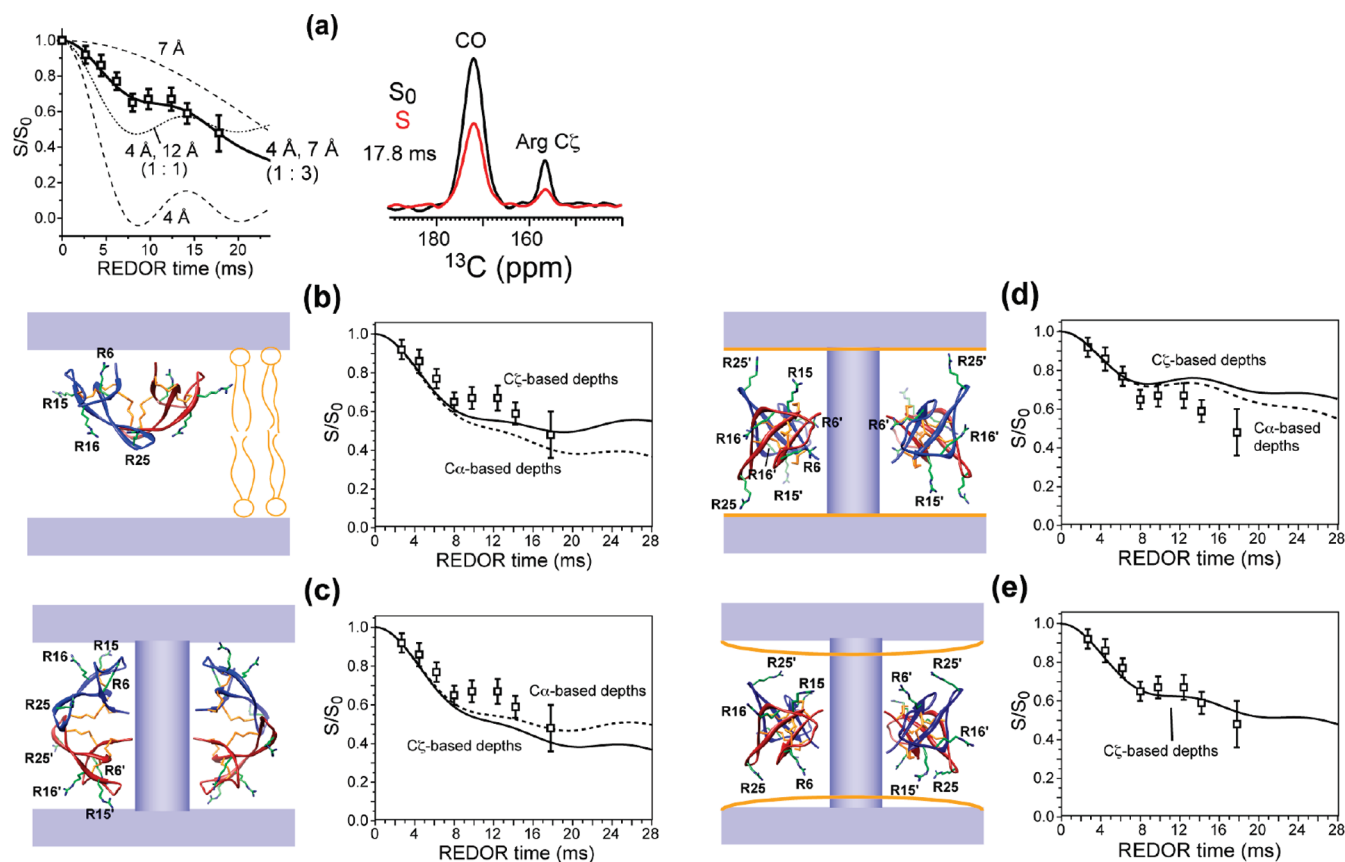


FIGURE 6: Arg $\text{C}\zeta$ - ^{31}P distances of HNP-1 in DMPC/DMPG bilayers. (a) $\text{C}\zeta$ ^{13}C - ^{31}P REDOR S/S_0 values as a function of mixing time and representative S_0 and S spectra. The best-fit simulation used a 1:3 combination of a 4 Å distance and a 7 Å distance. (b–e) Solid lines represent REDOR simulations using $\text{C}\zeta$ -P distances based on the vertical distance differences among the four Arg $\text{C}\zeta$ atoms. Dashed lines represent simulations based on the Arg $\text{C}\alpha$ vertical distance differences. (b) Membrane-immersed wedge model and the best-fit Arg $\text{C}\zeta$ -P REDOR curve. Simulated curves decay faster than the experimental data. (c) General pore model and best-fit $\text{C}\zeta$ -P curves, which decay faster than the measured data. (d and e) Simulation of the Arg $\text{C}\zeta$ -P REDOR data using the dimer pore model. (d) Dimer pore model based on the crystal structure of HNP-3 and a bilayer thickness of 35 Å. The simulated $\text{C}\zeta$ -P REDOR curves decay slower than the experimental data. (e) Dimer pore model after adjustment of the Arg side chain rotameric states (Table 1) with a membrane thickness of 30 Å. The calculated $\text{C}\zeta$ -P curve fits the data very well.

closest to the membrane surface, with their $\text{C}\zeta$ depths differing by only ~ 2 Å when the axis of the basket-shaped dimer is oriented parallel to the bilayer normal (Table 1) (12). Thus, if R6 $\text{C}\zeta$ is 4 Å from ^{31}P , then R15 $\text{C}\zeta$ should be ~ 6 Å distant. Using this approach, we estimated all four $\text{C}\zeta$ -P distances for the immersed wedge model (Table 1) and simulated the resulting REDOR curve. Figure 6b shows that the simulated REDOR curve decays faster than the experimental intensities, especially in the 8–14 ms regime.

Because Arg residues have multiple rotameric states with similar energetic stabilities (56) and the lipid bilayer is expected to exert a strong influence on the Arg side chain conformation through salt bridge formation (39, 57), the Arg side chains may adopt different conformations in the membrane and in the crystal. However, any rotamer differences should shorten the $\text{C}\zeta$ -P distances and accelerate the dipolar dephasing, rather than slowing the dephasing as required to fit the experimental data. When the four $\text{C}\zeta$ -P distances were estimated on the basis of the relative positions of the four Arg backbone $\text{C}\alpha$ atoms to eliminate side chain conformational effects, the simulated REDOR curve (dashed line) (Figure 6b) still decayed too fast compared to the observed data.

In the general pore model (Figure 6c), more than one Arg side chain was close to the ^{31}P atoms. Specifically, R6, R15, and R16 all have similar $\text{C}\zeta$ depths based on the crystal structure (Table 1) (12). Keeping the least inserted R15 $\text{C}\zeta$ -P distance

at 4 Å, as constrained by the REDOR data, we obtained R16 and R6 $\text{C}\zeta$ -P distances of ~ 6 and 7 Å, respectively. The resulting REDOR curve again decays faster than the measured data and cannot be remedied by changing the side chain conformations.

Finally, we considered the dimer pore model, in which the dimer orientation was rotated by 90° from that of the general pore model (Figure 6d). Here the situation is qualitatively different: R25 is now closest to the membrane surface, with the next nearest Arg, R15 in the other monomer, ~ 4 Å deeper in the membrane. Using the rotamers in the HNP-3 structure, we found the simulated curve to now decay more slowly than the measured data (Figure 6d), thus allowing us to modify the side chain conformations to minimize the $\text{C}\zeta$ -P distances. In addition, ^{13}CO - ^{31}P and $^{13}\text{C}\alpha$ - ^{31}P REDOR data suggested a slight membrane thinning from 35 to 30 Å (Figure 7). Combining these two changes, we obtained Arg rotamers that gave $\text{C}\zeta$ -P distances of 4, 6.5, 9, and 10 Å (Table 1), which gave excellent fit to the experimental data (Figure 6e). Moreover, R25, the residue with the shortest $\text{C}\zeta$ -P distance, is also the residue showing significant immobilization upon membrane binding (Figure 3). Thus, the conformational changes also support the dimer pore topology of HNP-1.

Distances from backbone CO and $\text{C}\alpha$ atoms to ^{31}P are consistent with the Arg $\text{C}\zeta$ REDOR data. Both signals decay slowly, with average S/S_0 values of ~ 0.8 at 14 ms. Simulations yielded average distances of 7.6 Å for CO atoms and 7.2 Å for

Table 1: Distances from Arg C ζ Atoms to Lipid ^{31}P Atoms (R_{CP} , angstroms) in Various Topology Models of HNPs in Lipid Bilayers

residue ^a	original HNP-3 structure ^b with a bilayer thickness of 35 Å			Arg-modified structure with a bilayer thickness of 30 Å		
	rotamer ^c	R_{CP} , wedge	R_{CP} , general pore	R_{CP} , dimer pore	rotamer	R_{CP} , dimer pore
R6	mmt180, mtt-85	4	7	15	tpt180	9
R15	mtt180	6	4	8	mtt85	6.5
R16	ttt180	16	6	16	ptt85	10
R25	mtt-85	18	15	4	ttt180	4

^aEach residue in principle has four distances to the membrane surfaces because of the dimer state and two bilayer surfaces. Tabulated here are the shortest distances, which are those relevant for the ^{13}C – ^{31}P distance experiment. ^bThe crystal structure of HNP-3 was used to model the dimer pore (12), because the NMR structure is for the HNP-1 monomer and has a lower resolution for the side chains. ^cThe symbols m, t, and p indicate -60° , 180° , and 60° , respectively, for the consecutive χ torsion angles from the backbone (56).

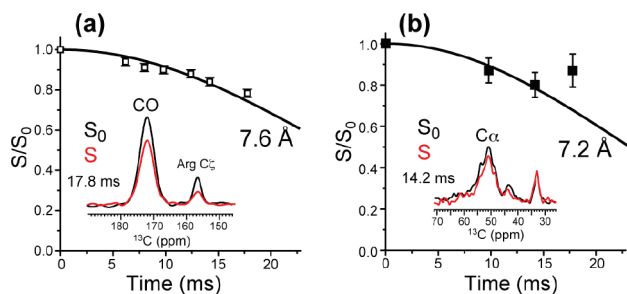


FIGURE 7: ^{13}C – ^{31}P REDOR dephasing of backbone CO and C α atoms of membrane-bound HNP-1: (a) CO peak and (b) C α peak. Best-fit curves represent average two-spin distances.

C α atoms. Because no site resolution was attempted, we added the REDOR dephasing of every CO and C α atom in each structural model based on their distances to the membrane surface. Figure S2 of the Supporting Information shows the distance distribution for the dimer pore model, where the shortest distance to ^{31}P was fixed at 4 Å. The simulated REDOR curves fit the measured dephasing well. In reaching this agreement, it was necessary to thin the membrane to 30 Å, suggesting that HNP-1 insertion slightly reduces the bilayer thickness. Although the backbone ^{13}C – ^{31}P REDOR did not exclude the other structural models, it was consistent with the dimer pore structure. In addition, the ^{13}CO – ^{31}P REDOR data verified that HNP-1 was inserted into the gel-phase membrane: simulations using a surface-bound wedge model were inconsistent with the experimental result (Figure S3 of the Supporting Information).

Residue-Specific Water–Protein Distances. To complement the topology information from the lipid–protein ^1H spin diffusion experiment, we examined the water–protein ^1H spin diffusion profile with a short mixing time of 2.2 ms, when the ^1H magnetization has not equilibrated in the protein, thus giving residue-specific information about water proximities. Figure 8a shows the water-edited ^{13}C spectrum (red) extracted from the water ^1H cross section of the 2D spectrum. This water-edited spectrum was superimposed with the ^{13}C CP spectrum that reflects the equilibrium ^{13}C magnetization. The two spectra were scaled such that the water-edited intensities at best equaled but never exceeded the CP intensities. It can be seen that the intensity distribution of the water-edited ^{13}C spectrum clearly differs from that of the CP spectrum, indicating selectivity of the water–protein spin diffusion at this mixing time. For example, the lipid chain signals from 33 to 22 ppm were significantly attenuated, as expected because of the immiscibility of water with the hydrocarbon core. The protein signals in the 40–53 ppm region, which mainly result from C α and C β , were also reduced compared to the C α intensities in the 55–60 ppm range.

To simulate the water-edited ^{13}C spectrum, we first reproduced the equilibrium CP spectrum by using appropriate weighting factors for each carbon. These weighting factors accounted for different CP dynamics of CH $_n$ ($n = 1, 2, \text{ or } 3$) groups and the different mobilities between the backbone and side chains (Figure 8b). Next, we assigned each carbon a spin diffusion weighting factor based on the proximity of each site to water on the membrane surface and water in the pore. Both the crystal structure of HNP-3 (12) and the solid-state NMR structure of HNP-1 (19) were considered in estimating the carbon–water distances, and the simulation was insensitive to the exact starting structure (Figure S4 of the Supporting Information). Three categories of spin diffusion weighting factors were used. Carbons close to water were given a weighting factor of 1 while those far from water a weighting factor of 0.1. Residues in the middle were assigned a weighting factor of 0.55. Combining the water-proximity weighting factors with the CP weighting factors, we simulated the water-edited spectrum expected for the dimer pore topology. Figure 8a shows that the simulated stick spectrum agrees well with the measured spectrum. The root-mean-square difference (rmsd) between the two was 0.22, normalized to the 54 ppm peak intensity (Figure 8c). This rmsd value is comparable to the experimental rms noise of 0.18, indicating that the measured spectrum is consistent with the dimer pore topology. We did not consider the intensities in the 22–33 ppm region because of the significant overlap between the lipid and protein signals.

Oligomeric Structure of HNP-1 in the Lipid Membrane. So far, we have assumed that HNP-1 assembles into a basic unit of dimers in the membrane, upon which loose higher-order oligomers may form. Although the immobilization result supports this assumption, we verified this hypothesis using the ^{19}F CODEX experiment, which detects ^{19}F magnetization exchange between orientationally different fluorinated molecules. The oligomeric number n is obtained from the equilibrium CODEX echo intensity of $1/n$ at long mixing times. Tyr4 in strand β 1 was replaced with 4- ^{19}F Phg, because crystal structures suggest this residue lies in the dimer interface, with intermonomer distances of less than 10 Å (Protein Data Bank entries 1DFN and 3HJ2). Figure 9 shows the ^{19}F CODEX control (S_0) and exchange (S) spectra of HNP-1 in DMPC/DMPG membranes (1:18 P:L ratio) at a mixing time of 1 s. The S/S_0 value was 0.66 ± 0.06 and was the same between 1 s and 500 ms within experimental uncertainty, indicating that intermolecular spin diffusion has equilibrated. The slightly larger than 0.5 final value indicates that the majority (66%) of Tyr4 exists in a dimer state ($n = 2$) while the rest (33%) has ^{19}F – ^{19}F distances of greater than ~ 15 Å. Thus, when the protein concentration is ~ 5 mol % in the membrane, the majority of HNP-1 is dimerized, while the rest

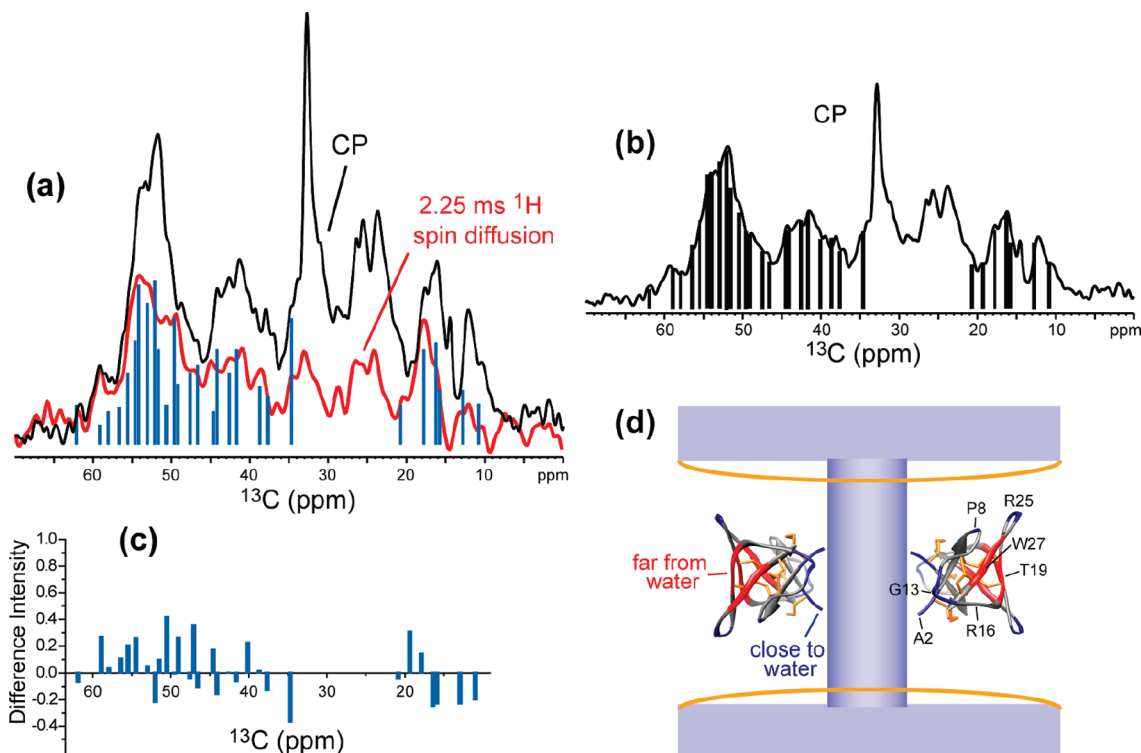


FIGURE 8: Water–protein ^1H spin diffusion to determine the membrane topology of HNP-1. (a) ^{13}C spectrum after 2.25 ms ^1H spin diffusion from water (red), superimposed with the ^{13}C CP spectrum (black). The simulated stick spectrum based on the dimer pore model is colored blue. (b) ^{13}C CP spectrum and simulation to fix the CP weighting factors. (c) Difference between the experimental and simulated water-edited spectrum from panel a. (d) Dimer pore model, in which residues close to water are colored blue, interfacial residues gray, and residues far from water red. The respective intensity weighting factors are 1, 0.55, and 0.1, respectively.

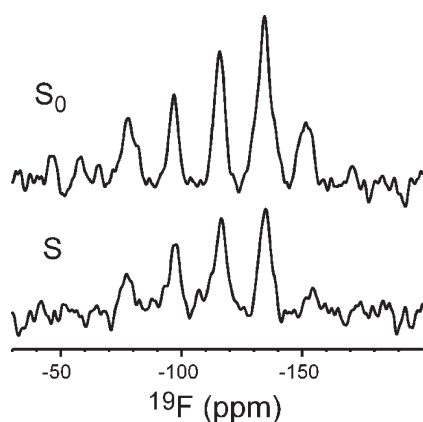


FIGURE 9: ^{19}F CODEX control (S_0) and dephased (S) spectra of 4- $[^{19}\text{F}]\text{Phg}_4$ HNP-1 in DMPC/DMPG (3:1) membranes at a 1:18 P:L ratio. The mixing time was 1 s. The S/S_0 value was 0.66 ± 0.06 .

either exists in a monomer state or forms loose dimers with Tyr4 separations greater than the detection limit of this ^{19}F spin diffusion technique.

DISCUSSION

Evidence of Pore Formation by HNPs in Lipid Membranes from Biochemical Data. Since the discovery of human α -defensins (3, 4), many antimicrobial assays, lipid vesicle experiments, and high-resolution structures have been reported with the aim of understanding the mechanisms of action of these host-defense proteins (1, 58). Similar to that of smaller β -hairpin antimicrobial peptides, the bactericidal activity of HNPs followed inner membrane permeabilization (59). Dye release and

fluorescence spectroscopy experiments found that HNP-1 caused both fusion and lysis of negatively charged lipid vesicles through electrostatic interactions (60). For rabbit neutrophil defensins, vesicle leakage depends on the membrane composition: it is all or none for whole *E. coli* lipids but graded for POPG vesicles (61). Electron micrographs of human parasite *Trypanosoma cruzi* cells in the presence of micromolar concentrations of HNP-1 showed distinct 25 nm sized pores in the cellular and flagellar membranes (62), through which HNP-1 appears to enter the trypanosome cells, causing subsequent DNA fragmentation and cell destruction. Vesicle leakage experiments also showed that HNP-induced pores increase in number with the concentration of the anionic lipid (63). These biochemical studies all indicate pore formation by human α -defensins in anionic lipid membranes. However, the exact structure and topology of HNP-1 at the pore and the type of lipid disorder have remained elusive.

Structural Constraints on HNP-1-Induced Pores in Anionic Lipid Membranes. The ^1H spin diffusion, ^{13}C – ^{31}P distances, and ^{19}F spin diffusion results gave the following constraints to HNP-1 structure in the anionic lipid membrane. At high protein concentrations (1:18 P:L ratios), HNP-1 fully spans the membrane and contacts the hydrophobic chains. Among the four Arg residues, one Arg forms hydrogen-bonded complexes with the lipid phosphates. This Arg is most likely R25 located near the $\beta 2$ – $\beta 3$ turn, because its signal was enhanced in the 2D spectra by lipid-induced immobilization. The DMPC/DMPG bilayer is thinned slightly upon HNP-1 binding. Seen at Tyr₄, the majority of the protein is at least dimerized at a 1:18 P:L ratio. These observations support the dimer pore model for HNP-1 (Figure 6d). The fully immersed wedge model (Figure 1c) and the general pore model (Figure 1e) would place R25 as the farthest Arg from the

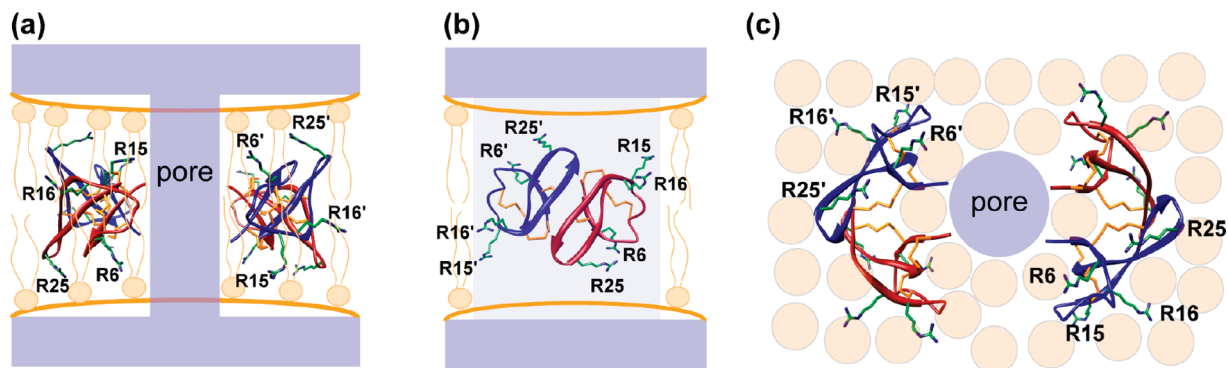


FIGURE 10: Membrane topology of HNP-1 in anionic lipid bilayers. At high protein concentrations, HNP-1 is mostly dimerized and spans the membrane, lining a central water pore. The R25 side chain lies closest to the membrane surface interacting with the phosphate groups. The lipid chains near the pore do not exhibit significant disorder: (a) side view, (b) 90° rotated side view from panel a, showing the pore behind one dimer, and (c) top view. The distances between the two dimers and the total oligomeric number of the assembly are not probed by the experiments described here.

membrane surface, which is inconsistent with the 2D ^{13}C spectra, because the hydrocarbon core is the most fluid region of the lipid bilayer and should not immobilize R25. The depth distributions of the four Arg side chains in the fully immersed wedge and general pore models also do not agree with the stoichiometry that only one Arg C ζ is H-bonded to the lipid phosphates. On the other hand, the surface-bound wedge model (Figure 1b) does not agree with the fast ^1H spin diffusion from the lipid chains to the protein. In the multimeric pore model (Figure 1f), the Arg backbones lie at roughly the same depths in each lipid leaflet, with the two C α rings separated by ~ 16 Å. Thus, the C ζ atoms would be similarly close to the membrane surface ^{31}P , which does not agree with the distance distribution of the C ζ -P REDOR data. At lower protein concentrations (1:40 P:L ratio), HNP-1 is less inserted into the membrane, as manifested by the slower lipid-to-protein ^1H spin diffusion. Although sensitivity limitations preclude the determination of the exact topology, we expect the surface-bound wedge model to be the most likely scenario at lower protein concentrations.

In model-specific fitting of the various experimental data, we primarily used the crystal structure of HNP-3 (Protein Data Bank entry 1DFN) because the solid-state NMR structure (19) (Protein Data Bank entry 2KHT) is that of the monomer, with no direct intermolecular constraints for the dimer. Nevertheless, Figure S4 of the Supporting Information shows that the hypothetical dimer NMR structure would give conclusions similar to those for the HNP-3 crystal structure for the water-edited ^{13}C spectrum, suggesting that the exact input structure does not affect the conclusion of the global topology of HNP-1.

Taken together, the solid-state NMR data shown here indicate a dimer pore topology of HNP-1, in which the β -sheet dimers span the membrane with the R25-containing $\beta 2$ - $\beta 3$ turn pointing toward the membrane surface (Figure 10). When water on the membrane surface and in the pore is considered, the dimer pore topology reproduces the observed water-edited protein ^{13}C spectrum. The ^{19}F spin diffusion data verify the dimerization of the majority of the protein. The small fraction of monomers is likely related to the observed shallower insertion of the protein at lower concentrations and suggests that concentration-dependent oligomerization may be important for the membrane-disruptive activity of HNP-1.

Does the dimer pore mechanism of HNP-1 apply to other human α -defensins? Comparisons of the activities and specificities of the six human α -defensins indicate that their interactions

with lipid membranes are diverse. Against Gram-positive *S. aureus*, the relative potencies were as follows: HNP-2 > HNP-1 > HNP-3 > HNP-4 (8). The relative potencies against the Gram-negative *E. coli* were as follows: HNP-4 > HNP-2 > HNP-1 = HNP-3 (8). Among HNP-1, -2, and -3, whose amino acid sequences differ only in their N-terminal residue, HNP-3, which possesses an N-terminal polar residue Asp, has weaker activities than HNP-1 and HNP-2, which have a hydrophobic N-terminal residue (5, 8). Consistently, acetylation and amidation of HNP-2 to remove the terminal charges modulated the protein's antimicrobial activity and vesicle leakage (64). Thus, the density and distribution of the positive charge have a significant effect on the membrane interaction of HNPs. In comparison, HD5 and HD6, which are found in intestinal epithelial cells, have much lower degrees of sequence homology to HNPs (6, 7). HD6 has activities nearly 2 orders of magnitude weaker than those of HNPs (8), while HD5, while localized on the cell membrane, was suggested to interact with the cells in a receptor-mediated fashion (65). On the basis of the high degree of sequence homology and functional similarity between HNP-1 and HNP-2, we speculate that the dimer pore mechanism may apply to HNP-2 and should be relevant to HNP-3 as well, but the other defensins in this family may adopt different orientations and insertions in the lipid membrane.

Comparison of HNP-1 with Small β -Hairpin Antimicrobial Peptides. Our previous studies of the two-stranded disulfide-bonded β -hairpin antimicrobial peptide, PG-1, indicated that the strong interactions between Arg guanidinium ions and the lipid phosphate groups drove the formation of toroidal pore defects in the membrane, where PG-1 lines the pore as a TM β -barrel (24, 39, 55). When the guanidinium ions were dimethylated, the mutant exhibited 3-fold weaker antimicrobial activities and no longer formed large β -barrels in the membrane (66). A PG-1 mutant with only half the number of Arg residues inserted only partly into the anionic membrane and exhibited much weaker interactions with the lipid headgroups (50). Guanidinium-phosphate interactions were also observed in two Arg-rich cell-penetrating peptides, penetratin (67) and the HIV TAT peptide (68). In HNP-1, although only one guanidinium ion is within H-bonding distance of the lipid phosphates, the average distance for the other three Arg residues is 7 Å, which is short compared to the bilayer thickness (Figure 6a). Lu and co-workers have shown by mutagenesis that when three of the four Arg residues were converted to Lys, HNP-1 activity was significantly weakened,

and the effect was more pronounced against the Gram-positive *S. aureus* than the Gram-negative *E. coli* (69).

It is interesting that no isotropic peak was observed in the ^{31}P NMR spectra, indicating that high-curvature defects such as micelles or toroidal pores were absent in the HNP-bound DMPC/DMPG membrane (Figure 2). Thus, in the DMPC/DMPG membrane, the HNP-1 dimer pores exist in regular lamellar bilayers, consistent with the classical barrel-stave model. The retention of the bilayer integrity contrasts with the behavior of PG-1, which caused substantial membrane disorder to phosphocholine (PC)/phosphatidylglycerol (PG) membranes as well as phosphatidylethanolamine (PE)/PG membranes. The interaction of HNP-1 with the DMPC/DMPG membrane is more akin to that of tachyplesins (70) and a synthetic antimicrobial arylamide (71), which did not disrupt PC/PG membranes. However, tachyplesin-1 caused clear disruption of the PE/PG membrane (70). The extent of membrane disorder depends on both the distribution of Arg residues in the protein sequence and the composition of the lipid membrane. It is possible that HNP-lipid interactions may be sensitive to the membrane composition, similar to tachyplesins, so that while HNP-1 does not disrupt PC/PG membranes, it may disrupt PE/PG membranes. Similarly, an increased percentage of the negatively charged PG lipids may increase the amount of membrane disorder. A study of rabbit neutrophil defensins suggested that the presence of PE and cardiolipin lipids increased the extent of membrane disruption (61). Given the increased complexity of HNPs over two-stranded β -hairpin antimicrobial peptides, structural investigations as a function of membrane composition will be useful to further elucidate the membrane interaction and mechanism of action of this class of defensins.

Finally, the precise antimicrobial mechanism of HNP-1 in vivo may depend on factors other than HNP-phospholipid interaction. It was recently reported that HNP-1 activity correlates with the amount of lipid II, a bacterial cell wall precursor (63); inhibition of lipid II synthesis weakened the HNP-1 antibacterial activity. This result suggests that interaction of cell wall components may be involved in the antimicrobial action of HNPs and may explain why D-amino acid analogues of HNPs appeared to have weaker bactericidal activities but similar membrane-disruptive abilities compared to those of their L-amino acid counterparts. Thus, the mechanism of action of HNPs, like a number of other defensins (72–75), may involve multiple targets in the bacteria. The dual mechanisms may also contribute to the lack of significant disorder seen in the ^{31}P NMR spectra.

SUPPORTING INFORMATION AVAILABLE

Additional 2D spectra and ^{13}C – ^{31}P REDOR analyses. This material is available free of charge via the Internet at <http://pubs.acs.org>.

REFERENCES

- Ganz, T. (2003) Defensins: Antimicrobial peptides of innate immunity. *Nat. Rev. Immunol.* 3, 710–720.
- Xie, C., Prahl, A., Ericksen, B., Wu, Z., Zeng, P., Li, X., Lu, W.-Y., Lubkowski, J., and Lu, W. (2005) Reconstruction of the Conserved β -Bulge in Mammalian Defensins Using D-Amino Acids. *J. Biol. Chem.* 280, 32921–32929.
- Selsted, M. E., Harwig, S. S., Ganz, T., Schilling, J. W., and Lehrer, R. I. (1985) Primary structures of three human neutrophil defensins. *J. Clin. Invest.* 76, 1436–1439.
- Gabay, J. E., Scott, R. W., Campanelli, D., Griffith, J., Wilde, C., Marra, M. N., Seeger, M., and Nathan, C. F. (1989) Antibiotic proteins of human polymorphonuclear leukocytes. *Proc. Natl. Acad. Sci. U.S.A.* 86, 5610–5614.
- Ganz, T., Selsted, M. E., Szklarek, D., Harwig, S. S., Daher, K., Bainton, D. F., and Lehrer, R. I. (1985) Defensins. Natural peptide antibiotics of human neutrophils. *J. Clin. Invest.* 76, 1427–1435.
- Jones, D. E., and Bevins, C. L. (1993) Defensin-6 mRNA in human Paneth cells: Implications for antimicrobial peptides in host defense of the human bowel. *FEBS Lett.* 315, 187–192.
- Jones, D. E., and Bevins, C. L. (1992) Paneth cells of the human small intestine express an antimicrobial peptide gene. *J. Biol. Chem.* 267, 23216–23225.
- Ericksen, B., Wu, Z., Lu, W., and Lehrer, R. I. (2005) Antibacterial activity and specificity of the six human α -defensins. *Antimicrob. Agents Chemother.* 49, 269–275.
- Wu, Z., Ericksen, B., Tucker, K., Lubkowski, J., and Lu, W. (2004) Synthesis and characterization of human α -defensins 4–6. *J. Pept. Res.* 64, 118–125.
- Lehrer, R. I., and Ganz, T. (1999) Antimicrobial peptides in mammalian and insect host defence. *Curr. Opin. Immunol.* 11, 23.
- Kagan, B. L., Selsted, M. E., Ganz, T., and Lehrer, R. I. (1990) Antimicrobial defensin peptides form voltage-dependent ion-permeable channels in planar lipid bilayer membranes. *Proc. Natl. Acad. Sci. U.S.A.* 87, 210–214.
- Hill, C. P., Yee, J., Selsted, M. E., and Eisenberg, D. (1991) Crystal structure of defensin HNP-3, an amphiphilic dimer: Mechanisms of membrane permeabilization. *Science* 251, 1481–1485.
- Szyk, A., Wu, Z., Tucker, K., Yang, D., Lu, W., and Lubkowski, J. (2006) Crystal structures of human α -defensins HNP4, HD5, and HD6. *Protein Sci.* 15, 2749–2760.
- Wimley, W. C., Selsted, M. E., and White, S. H. (1994) Interactions between human defensins and lipid bilayers: Evidence for formation of multimeric pores. *Protein Sci.* 3, 1362–1373.
- Luo, W., Yao, X. L., and Hong, M. (2005) Large Structure Rearrangement of Colicin Ia Channel Domain After Membrane Binding from 2D ^{13}C Spin Diffusion NMR. *J. Am. Chem. Soc.* 127, 6402–6408.
- Huster, D., Xiao, L. S., and Hong, M. (2001) Solid-state NMR investigation of the dynamics of colicin Ia channel-forming domain. *Biochemistry* 40, 7662–7674.
- Huster, D., Yao, X., Jakes, K., and Hong, M. (2002) Conformational changes of colicin Ia channel-forming domain upon membrane binding: A solid-state NMR study. *Biochim. Biophys. Acta* 1561, 159–170.
- Li, S., Zhang, Y., and Hong, M. (2010) 3D ^{13}C – ^{13}C correlation NMR for de novo distance determination of solid proteins and application to a human α -defensin. *J. Magn. Reson.* 202, 203–210.
- Zhang, Y., Doherty, T., Li, J., Lu, W., Barinka, C., Lubkowski, J., and Hong, M. (2010) Resonance assignment and three-dimensional structure determination of a human α -defensin, HNP-1, by solid-state NMR. *J. Mol. Biol.* 397, 408–422.
- Luo, W., and Hong, M. (2006) Determination of the oligomeric number and intermolecular distances of membrane protein assemblies by anisotropic ^1H -driven spin diffusion NMR spectroscopy. *J. Am. Chem. Soc.* 128, 7242–7251.
- Luo, W., Mani, R., and Hong, M. (2007) Sidechain conformation and gating of the M2 transmembrane peptide pore channel of influenza A virus from solid-state NMR. *J. Phys. Chem.* 111, 10825–10832.
- Pazgier, M., and Lubkowski, J. (2006) Expression and purification of recombinant human α -defensins in *Escherichia coli*. *Protein Expression Purif.* 49, 1–8.
- Wu, Z., Powell, R., and Lu, W. (2003) Productive folding of human neutrophil α -defensins in vitro without the pro-peptide. *J. Am. Chem. Soc.* 125, 2402–2403.
- Mani, R., Cady, S. D., Tang, M., Waring, A. J., Lehrer, R. I., and Hong, M. (2006) Membrane-dependent oligomeric structure and pore formation of a β -hairpin antimicrobial peptide in lipid bilayers from solid-state NMR. *Proc. Natl. Acad. Sci. U.S.A.* 103, 16242–16247.
- Afonin, S., Glaser, R. W., Berditchevskaia, M., Wadhvani, P., Guhrs, K. H., Mollmann, U., Perner, A., and Ulrich, A. S. (2003) 4-Fluorophenylglycine as a label for ^{19}F NMR structure analysis of membrane-associated peptides. *ChemBioChem* 4, 1151–1163.
- Zou, G., de Leeuw, E., Lubkowski, J., and Lu, W. (2008) Molecular determinants for the interaction of human neutrophil α -defensin 1 with its propeptide. *J. Mol. Biol.* 381, 1281–1291.
- Takegoshi, K., Nakamura, S., and Terao, T. (2001) ^{13}C - ^1H dipolar-assisted rotational resonance in magic-angle spinning NMR. *Chem. Phys. Lett.* 344, 631–637.
- Rienstra, C. M., Hohwy, M., Hong, M., and Griffin, R. G. (2000) 2D and 3D ^{15}N - ^{13}C - ^{13}C NMR chemical shift correlation spectroscopy of solids: Assignment of MAS spectra of peptides. *J. Am. Chem. Soc.* 122, 10979–10990.

29. Hong, M. (1999) Resonance Assignment of $^{13}\text{C}/^{15}\text{N}$ Labeled Proteins by Two- and Three-Dimensional Magic-Angle-Spinning NMR. *J. Biomol. NMR* 15, 1–14.
30. Baldus, M., Petkova, A. T., Herzfeld, J., and Griffin, R. G. (1998) Cross polarization in the tilted frame: Assignment and spectral simplification in heteronuclear spin systems. *Mol. Phys.* 95, 1197–1207.
31. Munowitz, M. G., Griffin, R. G., Bodenhausen, G., and Huang, T. H. (1981) Two-dimensional rotational spin-echo NMR in solids: Correlation of chemical shift and dipolar interactions. *J. Am. Chem. Soc.* 103, 2529–2533.
32. Rhim, W.-K., Elleman, D. D., and Vaughan, R. W. (1973) Analysis of multiple-pulse NMR in solids. *J. Chem. Phys.* 59, 3740–3749.
33. Hong, M., and Griffin, R. G. (1998) Resonance Assignment for Solid Peptides by Dipolar-Mediated $^{13}\text{C}/^{15}\text{N}$ Correlation Solid-State NMR. *J. Am. Chem. Soc.* 120, 7113–7114.
34. Rienstra, C., Tucker-Kellogg, L., Jaroniec, C., Hohg, M., Reif, B., McMahon, M., Tidor, B., Lozano-Pérez, T., and Griffin, R. (2002) De novo determination of peptide structure with solid-state magic-angle spinning NMR spectroscopy. *Proc. Natl. Acad. Sci. U.S.A.* 99, 10260–10265.
35. Mehring, M. (1983) High Resolution NMR in Solids, Springer-Verlag, New York.
36. Huster, D., Yao, X. L., and Hong, M. (2002) Membrane protein topology probed by ^1H spin diffusion from lipids using solid-state NMR spectroscopy. *J. Am. Chem. Soc.* 124, 874–883.
37. Kumashiro, K. K., Schmidt-Rohr, K., Murphy, O. J., Ouellette, K. L., Cramer, W. A., and Thompson, L. K. (1998) A novel tool for probing membrane protein structure: Solid-state NMR with proton spin diffusion and X-nucleus detection. *J. Am. Chem. Soc.* 120, 5043–5051.
38. Jaroniec, C. P., Tounge, B. A., Rienstra, C. M., Herzfeld, J., and Griffin, R. G. (1999) Measurement of ^{13}C - ^{15}N distances in uniformly ^{13}C labeled biomolecules: J-decoupled REDOR. *J. Am. Chem. Soc.* 121, 10237–10238.
39. Tang, M., Waring, A. J., and Hong, M. (2007) Phosphate-Mediated Arginine Insertion into Lipid Membranes and Pore Formation by a Cationic Membrane Peptide from Solid-State NMR. *J. Am. Chem. Soc.* 129, 11438–11446.
40. deAzevedo, E. R., Bonagamba, T. J., Hu, W., and Schmidt-Rohr, K. (1999) Centerband-only detection of exchange: Efficient analysis of dynamics in solids by NMR. *J. Am. Chem. Soc.* 121, 8411–8412.
41. Buffy, J. J., Waring, A. J., and Hong, M. (2005) Determination of Peptide Oligomerization in Lipid Membranes with Magic-Angle Spinning Spin Diffusion NMR. *J. Am. Chem. Soc.* 127, 4477–4483.
42. Wang, Y., and Jardetzky, O. (2002) Probability-based protein secondary structure identification using combined NMR chemical-shift data. *Protein Sci.* 11, 852–861.
43. Cady, S. D., Goodman, C., Tatko, C., DeGrado, W. F., and Hong, M. (2007) Determining the orientation of uniaxially rotating membrane proteins using unoriented samples: A ^2H , ^{13}C , and ^{15}N solid-state NMR investigation of the dynamics and orientation of a transmembrane helical bundle. *J. Am. Chem. Soc.* 129, 5719–5729.
44. Hong, M., and Doherty, T. (2006) Orientation determination of membrane-disruptive proteins using powder samples and rotational diffusion: A simple solid-state NMR approach. *Chem. Phys. Lett.* 432, 296–300.
45. Aisenbrey, C., and Bechinger, B. (2004) Investigations of polypeptide rotational diffusion in aligned membranes by ^2H and ^{15}N solid-state NMR spectroscopy. *J. Am. Chem. Soc.* 126, 16676–16683.
46. Lewis, B. A., Harbison, G. S., Herzfeld, J., and Griffin, R. G. (1985) NMR structural analysis of a membrane protein: Bacteriorhodopsin peptide backbone orientation and motion. *Biochemistry* 24, 4671–4679.
47. Fares, C., Qian, J., and Davis, J. H. (2005) Magic angle spinning and static oriented sample NMR studies of the relaxation in the rotating frame of membrane peptides. *J. Chem. Phys.* 122, 194908.
48. Hoover, D. M., Rajashankar, K. R., Blumenthal, R., Puri, A., Oppenheim, J. J., Chertov, O., and Lubkowsky, J. (2000) The structure of human β -defensin-2 shows evidence of higher order oligomerization. *J. Biol. Chem.* 275, 32911–32918.
49. Schmidt-Rohr, K., and Spiess, H. W. (1994) Multidimensional Solid-State NMR and Polymers, 1st ed., Academic Press, San Diego.
50. Tang, M., Waring, A. J., and Hong, M. (2009) Effects of arginine density on the membrane-bound structure of a cationic antimicrobial peptide from solid-state NMR. *Biochim. Biophys. Acta* 1788, 514–521.
51. Huang, H. W. (2000) Action of antimicrobial peptides: Two-state model. *Biochemistry* 39, 8347–8352.
52. Glaser, R. W., Sachse, C., Durr, U. H., Wadhvani, P., Afonin, S., Strandberg, E., and Ulrich, A. S. (2005) Concentration-Dependent Realignment of the Antimicrobial Peptide PGLa in Lipid Membranes Observed by Solid-State ^{19}F -NMR. *Biophys. J.* 88, 3392–3397.
53. Hong, M. (2007) Structure, topology, and dynamics of membrane peptides and proteins from solid-state NMR spectroscopy. *J. Phys. Chem. B* 111, 10340–10351.
54. Hong, M. (2006) Oligomeric structure, dynamics, and orientation of membrane proteins from solid-state NMR. *Structure* 14, 1731–1740.
55. Tang, M., and Hong, M. (2009) Structure and mechanism of β -hairpin antimicrobial peptides in lipid bilayers from solid-state NMR spectroscopy. *Mol. Biosyst.* 5, 317–322.
56. Lovell, S. C., Word, J. M., Richardson, J. S., and Richardson, D. C. (2000) The penultimate rotamer library. *Proteins: Struct., Funct., Genet.* 40, 389–408.
57. Schug, K. A., and Lindner, W. (2005) Noncovalent binding between guanidinium and anionic groups: Focus on biological- and synthetic-based arginine/guanidinium interactions with phosph[on]ate and sulf[on]ate residues. *Chem. Rev.* 105, 67–114.
58. Lehrer, R. I., Lichtenstein, A. K., and Ganz, T. (1993) Defensins: Antimicrobial and cytotoxic peptides of mammalian cells. *Annu. Rev. Immunol.* 11, 105–128.
59. Lehrer, R. I., Barton, A., Daher, K. A., Harwig, S. S., Ganz, T., and Selsted, M. E. (1989) Interaction of human defensins with *Escherichia coli*. Mechanism of bactericidal activity. *J. Clin. Invest.* 84, 553–561.
60. Fujii, G., Selsted, M. E., and Eisenberg, D. (1993) Defensins promote fusion and lysis of negatively charged membranes. *Protein Sci.* 2, 1301–1312.
61. Hristova, K., Selsted, M. E., and White, S. H. (1997) Critical role of lipid composition in membrane permeabilization by rabbit neutrophil defensins. *J. Biol. Chem.* 272, 24224–24233.
62. Madison, M. N., Kleshchenko, Y. Y., Nde, P. N., Simmons, K. J., Lima, M. F., and Villalta, F. (2007) Human Defensin α -1 Causes *Trypanosoma cruzi* Membrane Pore Formation and Induces DNA Fragmentation, Which Leads to Trypanosome Destruction. *Infect. Immun.* 75, 4780–4791.
63. de Leeuw, E., Li, C., Zeng, P., Li, C., Diepeveen-de Buin, M., Lu, W. Y., Breukink, E., and Lu, W. (2010) Functional interaction of human neutrophil peptide-1 with the cell wall precursor lipid II. *FEBS Lett.* 584, 1543–1548.
64. Xie, C., Zeng, P., Ericksen, B., Wu, Z., Lu, W.-Y., and Lu, W. (2005) Effects of the Terminal Charges in Human Neutrophil α -Defensin 2 on its Bactericidal and Membrane Activity. *Peptides* 26, 2377–2383.
65. de Leeuw, E., Rajabi, M., Zou, G., Pazgier, M., and Lu, W. (2009) Selective Arginines are Important for the Antibacterial Activity and Host Cell Interaction of Human α -defensin 5. *FEBS Lett.* 583, 2507–2512.
66. Tang, M., Waring, A. J., Lehrer, R. I., and Hong, M. (2008) Effects of Guanidinium-Phosphate Hydrogen Bonding on the Membrane-Bound Structure and Activity of an Arginine-Rich Membrane Peptide from Solid-State NMR. *Angew. Chem., Int. Ed.* 47, 3202–3205.
67. Su, Y., Doherty, T., Waring, A. J., Ruchala, P., and Hong, M. (2009) Roles of Arginine and Lysine Residues in the Translocation of a Cell-Penetrating Peptide from ^{13}C , ^{31}P and ^{19}F Solid-State NMR. *Biochemistry* 48, 4587–4595.
68. Su, Y., Waring, A. J., Ruchala, P., and Hong, M. (2010) Membrane-Bound Dynamic Structure of an Arginine-Rich Cell-Penetrating Peptide, the Protein Transduction Domain of HIV TAT, from Solid-State NMR. *Biochemistry* 49, 6009–6020.
69. Zou, G., de Leeuw, E., Li, C., Pazgier, M., Li, C., Zeng, P., Lu, W., Lubkowsky, J., and Lu, W. (2007) Toward understanding the cationicity of defensins. Arg and Lys versus their noncoded analogs. *J. Biol. Chem.* 282, 19653–19665.
70. Doherty, T., Waring, A. J., and Hong, M. (2006) Peptide-lipid interactions of the β -hairpin antimicrobial peptide tachyplesin and its linear derivatives from solid-state NMR. *Biochim. Biophys. Acta* 1758, 1285–1291.
71. Su, Y., DeGrado, W. F., and Hong, M. (2010) Orientation, dynamics, and lipid interaction of an antimicrobial arylamide investigated by ^{19}F and ^{31}P solid-state NMR spectroscopy. *J. Am. Chem. Soc.* 132, 9197–9205.
72. Christ, K., Wiedemann, I., Bakowsky, U., Sahl, H. G., and Bendas, G. (2007) The role of lipid II in membrane binding of and pore formation by nisin analyzed by two combined biosensor techniques. *Biochim. Biophys. Acta* 1768, 694–704.
73. Sass, V., Schneider, T., Wilmes, M., Körner, C., Tossi, A., Novikova, N., Shamova, O., and Sahl, H. G. (2010) Human β -defensin 3 inhibits cell wall biosynthesis in Staphylococci. *Infect. Immun.* 78, 2793–2800.

74. Schmitt, P., Wilmes, M., Pugnère, M., Aumelas, A., Bachère, E., Sahl, H. G., Schneider, T., and Destoumieux-Garzón, D. (2010) Insight into invertebrate defensin mechanism of action: Oyster defensins inhibit peptidoglycan biosynthesis by binding to lipid II. *J. Biol. Chem.* 285, 29208–29216.
75. Schneider, T., Kruse, T., Wimmer, R., Wiedemann, I., Sass, V., Pag, U., Jansen, A., Nielsen, A. K., Mygind, P. H., Raventos, D. S., Neve, S., Ravn, B., Bonvin, A. M., De Maria, L., Andersen, A. S., Gammelgaard, L., Sahl, H. G., and Kristensen, H. H. (2010) Plectasin, a fungal defensin, targets the bacterial cell wall precursor Lipid II. *Science* 328, 1168–1172.